Lithos 180–181 (2013) 252–263

Contents lists available at ScienceDirect

Lithos

journal homepage: www.elsevier.com/locate/lithos

Age distribution of lamproites along the Socovos Fault (southern Spain) and lithospheric scale tearing

Luis Alfonso Pérez-Valera [a,*], Gideon Rosenbaum [b], Mario Sánchez-Gómez [a], Antonio Azor [c], Juan Manuel Fernández-Soler [d,e], Fernando Pérez-Valera [a], Paulo M. Vasconcelos [b]

[a] Departamento de Geología, Universidad de Jaén, Campus Las Lagunillas s/n, 23071 Jaén, Spain
[b] School of Earth Sciences, The University of Queensland, Brisbane, Queensland 4072, Australia
[c] Departamento de Geodinámica, Universidad de Granada, Av. Fuentenueva s/n, 18071 Granada, Spain
[d] Departamento de Mineralogía y Petrología, Universidad de Granada, Av. Fuentenueva s/n, 18071 Granada, Spain
[e] Instituto Andaluz de Ciencias de la Tierra, CSIC & UGR, Avda. de Las Palmeras nº 4, 18100 Armilla, Granada, Spain

ARTICLE INFO

Article history:
Received 25 February 2013
Accepted 19 August 2013
Available online 29 August 2013

Keywords:
Lamproite
$^{40}Ar/^{39}Ar$ dating
Strike–slip fault
Tear fault
Betic Cordillera
Western Mediterranean

ABSTRACT

Lithospheric-scale tearing is commonly linked to the lateral termination of subduction rollback and slab segmentation. The upper-crustal expression of this process can be associated with the development of arcuate orogenic belts (oroclines) generated by a combination of vertical-axis block rotations and strike–slip faulting. However, the link between such strike–slip faults and slab tearing is relatively poorly constrained. We show here an example from the Gibraltar Arc in the westernmost Mediterranean, where lithospheric-scale tear faulting during the Late Miocene accommodated westward subduction rollback. The dextral strike–slip Socovos Fault in the eastern Betics may represent one of the surface expressions of this process. We document a high concentration of mantle-derived volcanic rocks (lamproites) along the Socovos Fault, which were intruded as dikes during the Late Miocene. Phlogopite and whole-rock $^{40}Ar/^{39}Ar$ ages of lamproites along the Socovos Fault show a spatial age zonation, with older ages (9.3–8.2 Ma) in the east and younger ages (7.3–7.1 Ma) in the west. This age distribution of the lamproites along the Socovos Fault is compatible with the westward retreat of the lithospheric slab that was active beneath the eastern Betics in the Late Miocene. We therefore hypothesize that tearing allowed pathways for lamproite melts in the subcontinental lithospheric mantle and lower crust, with the Socovos Fault channelizing these magmas in the upper crust.

1. Introduction

Tear faulting along sub-vertical planar structures is predicted to occur in response to subduction rollback at slab edges (e.g., Govers and Wortel, 2005; Hale et al., 2010; Rosenbaum et al., 2008). These structures are likely to act as transfer faults that propagate in the direction of subduction rollback. Their lithospheric-scale nature means that they can provide pathways for asthenospheric upwelling and upper mantle flow (e.g., Liu and Stegman, 2012; Schellart, 2004), thus generating localized magmatism in the area of tear faulting (Gasparon et al., 2009; Maury et al., 2000; Rosenbaum et al., 2008). Therefore, tracing the spatial and temporal distribution of tear-related magmatism could provide crucial information on the geodynamic history of convergent plate boundaries.

The formation of the Gibraltar Arc in the Betic-Rif orogenic belt (Fig. 1) has supposedly involved westward rollback accompanied by slab tearing (Duggen et al., 2008; Gutscher et al., 2012; Rosell et al., 2011; Rosenbaum and Lister, 2004). Westward rollback and slab tearing is supported by geophysical evidence, such as seismic tomography (Spakman and Wortel, 2004; Wortel and Spakman, 2000), deep electric resistivity (Rosell et al., 2011), and SKS splitting analysis (Bokelmann et al., 2011; Díaz et al., 2010). Rollback has triggered continental backarc extension in the Alborán Sea (Booth-Rea et al., 2007) and oroclinal bending by vertical-axis block rotations (Lonergan and White, 1997; Mattei et al., 2006, 2007). Possible active subduction beneath the Gibraltar Arc (Gutscher et al., 2002, 2012; Pedrera et al., 2011) is restricted to a narrow slab segment, with potential tear faulting occurring at the slab edges, beneath the Betics and Rif mountain chains (Govers and Wortel, 2005).

This paper focuses on the surface magmatic expression of slab tearing along the northern edge of the Gibraltar Arc. We present structural, geochemical and geochronological results from the Socovos Fault, which is a dextral strike–slip fault in the eastern Betics that may have accommodated some of the kinematics associated with westward subduction rollback. The Socovos Fault shows a large concentration of mantle-derived ultrapotassic dikes, which raises the question whether

* Corresponding author. Tel.: +34 953213056; fax: +34 953212946.
E-mail addresses: laperez@ujaen.es (L.A. Pérez-Valera), g.rosenbaum@uq.edu.au (G. Rosenbaum), msgomez@ujaen.es (M. Sánchez-Gómez), azor@ugr.es (A. Azor), jmfsoler@ugr.es (J.M. Fernández-Soler), fperez@ujaen.es (F. Pérez-Valera), p.vasconcelos@uq.edu.au (P.M. Vasconcelos).

0024-4937/$ – see front matter © 2013 Elsevier B.V. All rights reserved.
http://dx.doi.org/10.1016/j.lithos.2013.08.016

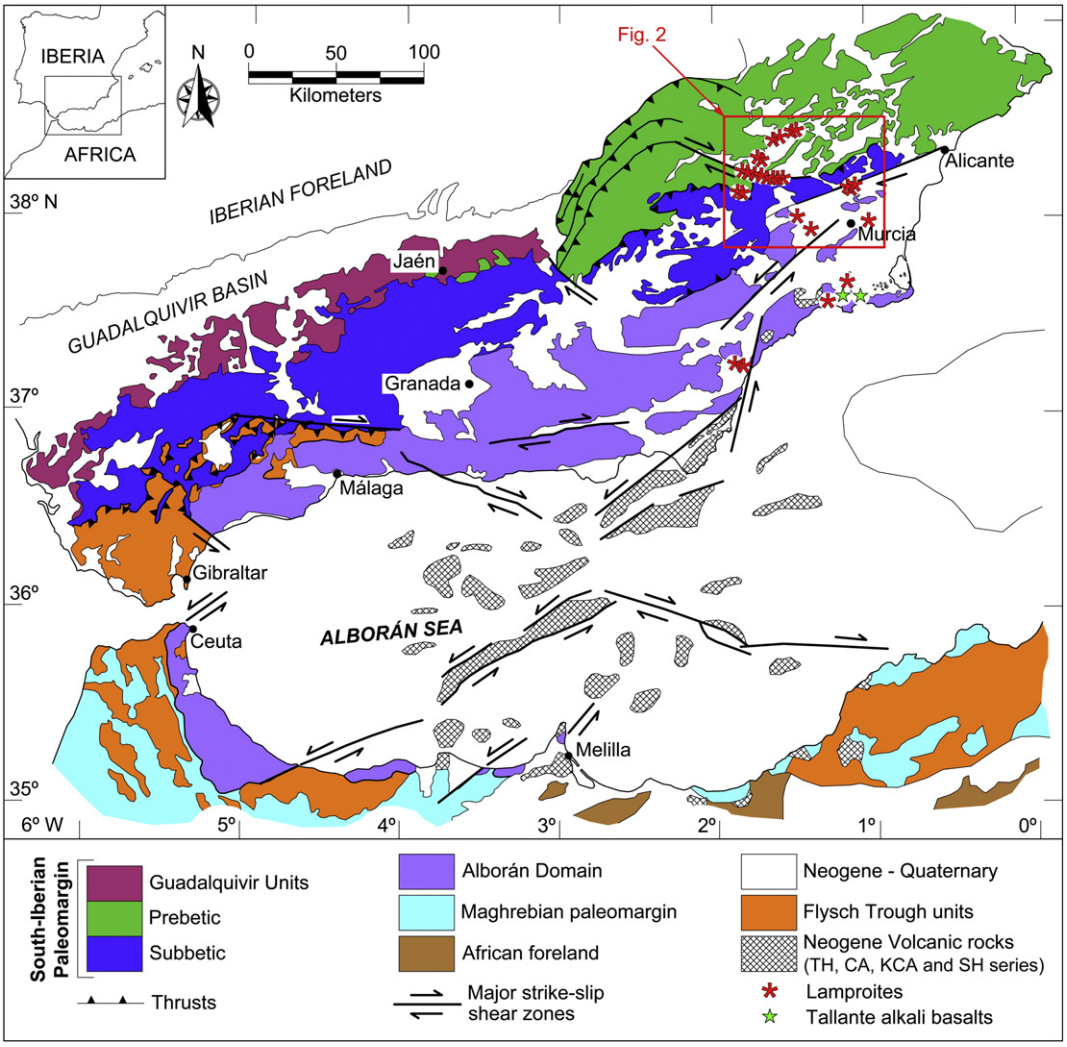

Fig. 1. Geological map of the Betic-Rif orogen (modified from Comas et al., 1999). Map also shows major strike–slip faults and shear zones, as well as lamproite outcrops.

the spatio-temporal distribution of magmatism was controlled by the fault geometry. To address this question, we provide new $^{40}Ar/^{39}Ar$ data on the timing of lamproitic magmatism. We then discuss these data in the context of the geochemistry of the lamproitic dikes, and the possibility that melt migration was assisted by the existence of a lithospheric tear fault underlying the Socovos Fault.

2. Geological setting

The Gibraltar Arc, in the westernmost Mediterranean, is depicted by the strongly curved Betic-Rif orogen, which wraps around the Alborán Sea (Fig. 1). Orogenesis occurred during Africa–Iberia convergence (Faccenna et al., 2004; Rosenbaum et al., 2002), combined with westward slab rollback and simultaneous back-arc extension in the Alborán Sea (Bokelmann et al., 2011; Booth-Rea et al., 2007; Duggen et al., 2008; Gutscher et al., 2002; Martínez-Martínez et al., 2006). Extensional tectonics that formed the Alborán Sea is also recognized in ductile and brittle structures within the Betics and Rif (Balanyá et al., 2012; Booth-Rea et al., 2007). In addition, slab tearing and/or slab detachment is evidenced by seismic imaging (e.g., Mancilla et al., 2013; Spakman and Wortel, 2004) and in the geochemistry of magmatic rocks (e.g., Duggen et al., 2008). The formation of the Betic-Rif orogen and Alborán Sea have been explained by a number of alternative geodynamic models (e.g. orogenic collapse, Platt et al., 2003b; Turner et al., 1999) but based on geochemical and geophysical data, the model involving subduction rollback, slab tearing and slab break-off provides the most consistent and well-constrained scenario (Bokelmann et al., 2011; Garcia-Castellanos and Villaseñor, 2011).

Deformation in the Betic-Rif orogen resulted from the collision of the Internal Zone (Alborán Domain) with the two External Zones (South-Iberian and Maghrebian paleomargins, Fig. 1), which constitute thin-skinned fold-and-thrust belts (e.g., Platt et al., 2013). The South-Iberian paleomargin is subdivided into two major domains, Subbetic and Prebetic Units, which consist of Mesozoic and Cenozoic sedimentary rocks. These rocks are unconformably overlain by Late Miocene to Quaternary sedimentary rocks, which are locally intruded by rocks of the SE Spain Volcanic Province (Fig. 1).

Strike-slip faults and shear zones that supposedly accommodated the westward emplacement of the Alborán Domain (Fig. 1) (Leblanc and Olivier, 1984), are generally sinistral in the Rif (e.g., Leblanc, 1990) and dextral in the Betics (Mattei et al., 2006; Platt et al., 2003a). In the central Betics, dextral strike–slip faulting acted as a transfer between two sectors undergoing active normal faulting (Martínez-Martínez et al., 2006). In the eastern Betics, the dextral Crevillente Fault accommodated the lateral displacement between the Alborán Domain and the South-Iberian paleomargin (Sanz de Galdeano and Buforn, 2005). Within the South-Iberian paleomargin, the dextral Socovos Fault represents a major structure (Platt et al., 2003a) with a length of more than 80 km and an average slip of 35 km in its central segment (Jerez-Mir, 1973). The Socovos Fault is characterized by a wide (~300 m) fault zone with cataclasites, foliated cataclasites and fault gouges. Two Mesozoic units with contrasting thicknesses (1–4 km and 8–10 km,

respectively) are placed side by side along the Socovos Fault, thus suggesting that the underlying Paleozoic basement was also faulted.

The Neogene volcanic province of SE Spain includes calc-alkaline (CA), high-K calc-alkaline (KCA), shoshonitic (SH) and ultrapotassic (UK) rocks, as well as alkali basalts (Benito et al., 1999). Due to geographical distribution and age younging from the CA to UK series, the volcanic rocks have been interpreted to be genetically linked (Benito et al., 1999; Duggen et al., 2005). Volcanism associated with the CA, KCA and SH series was emplaced only in the Alborán Domain (Fig. 1), while the UK rocks (lamproites) also intruded the South-Iberian paleomargin. The alkali basalts are younger (Duggen et al., 2005), and were interpreted as post-collisional anorogenic magmatism emplaced during the Pliocene (e.g., Beccaluva et al., 2011). Nevertheless, mantle xenoliths from the alkali basalts show a mantle metasomatic component that is also recognized in rocks of the SE Spain Volcanic Province (Beccaluva et al., 2004).

Ultrapotassic rocks from the SE Spain Volcanic Province seem to be spatially related to strike–slip faulting (Fig. 1). In particular, a large cluster of lamproitic dikes (27 dikes) and a volcanic edifice (Calasparra) were emplaced along the 25 km-long central segment of the Socovos Fault (Fig. 2). These dikes intruded along the main fault planes, as well as along secondary Riedel faults and tension gashes inside the fault zone, thus indicating an intimate link between faulting and volcanism (Pérez-Valera et al., 2010). The size of these dikes varies along the fault trace, with dikes in the western part being ~2 m thick and <300 m long, and those in the easternmost part reaching a thickness of up to 10 m and a length up to ~2 km. Sedimentary-derived xenoliths from the host rock are commonly found close to the dike limits. Nevertheless, deep-crustal xenoliths have been observed only in a few dikes emplaced east of Calasparra (Fig. 2). The easternmost dikes show a large proportion of granite and other crustal xenoliths.

The Socovos Fault was active at least since Middle Miocene as inferred from the relationship of Neogene sedimentation and faulting (Jerez-Mir, 1973). Some of the lamproitic rocks are faulted, striated or incorporated into the fault breccia, thus indicating that faulting also occurred after volcanism. A few segments of the Socovos Fault, including the one described here, show evidence for Quaternary activity (Sánchez-Gómez et al., 2011).

3. Analytical methods

3.1. Whole-rock and mineral analyses

Major elements was determined by XRF on fused Li-tetraborate beads at the Scientific Instrumentation Center of the University of

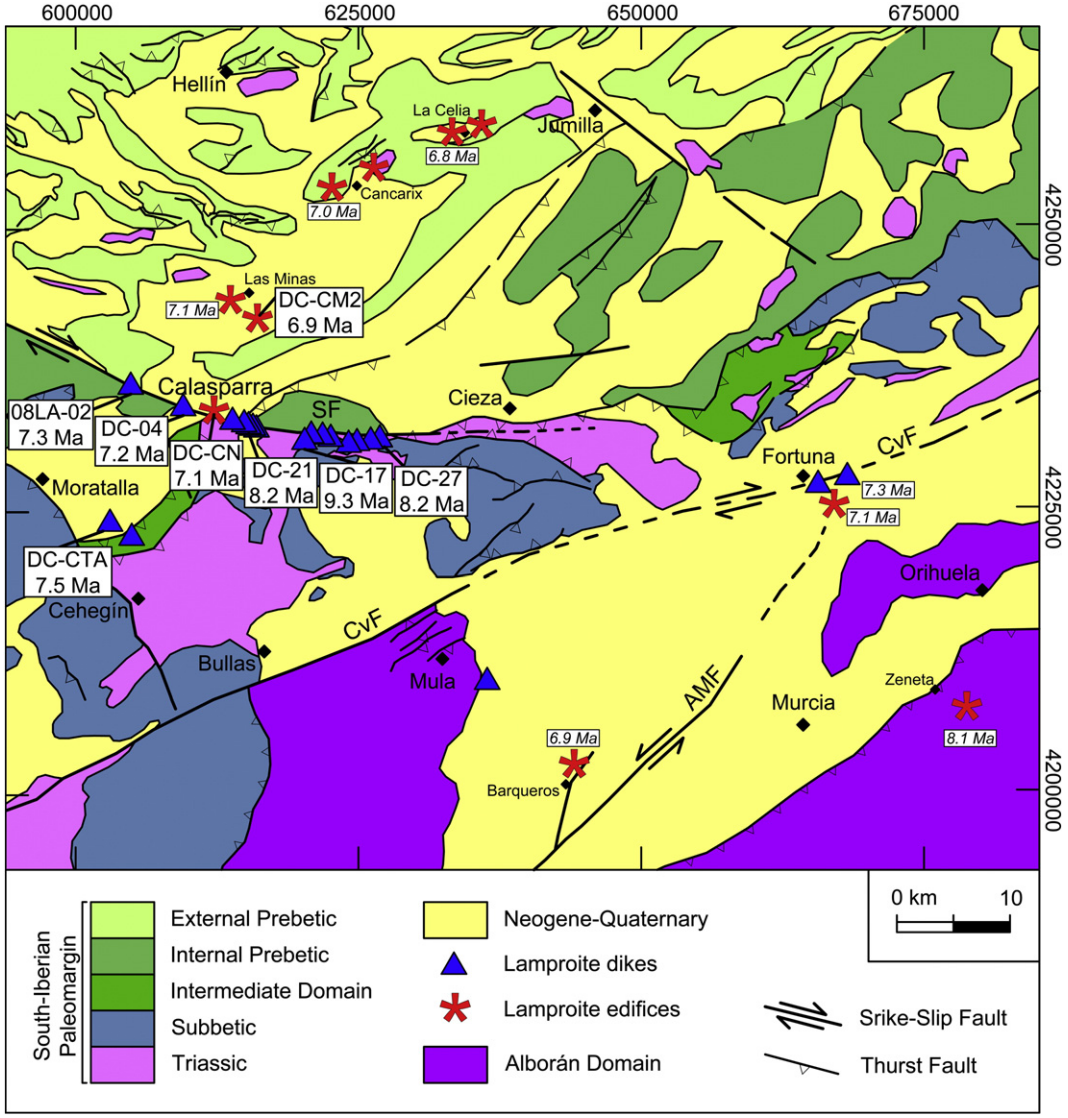

Fig. 2. Geological map of southeast Spain showing lamproite occurrences and major geological structures. New $^{40}Ar/^{39}Ar$ ages are shown with sample name. Also shown are published $^{40}Ar/^{39}Ar$ ages (from Duggen et al., 2005) in smaller italics letters. SF: Socovos Fault; CvF: Crevillente Fault; AMF: Alhama de Murcia Fault.

Granada (CIC-UGR), using a Panalytical MagiX Pro sequential spectrometer equipped with a Rh X-ray tube, which was calibrated using a large number of certified geological standards. Typical precision is better than 1.5% relative for concentration of 10%. Loss on ignition was determined gravimetrically as weight loss between 110 °C and 1000 °C. Zr was determined by XRF on pressed-power pellets, using Compton scattered radiation for matrix corrections. Detection limits for Zr are around 2–4 ppm. Other trace elements were determined by ICP-MS at the University of Granada (PE/Sciex Elan 5000), following dissolution of 0.1 g in concentrated HF-HNO_3 in Teflon lined vessels at high temperature and pressure in a microwave, evaporation to dryness, and final dilution to 100 mL of 4% HNO_3. Rh was used as an internal standard. Typical precision was better than 2% and 5% relative for analyte concentrations of 50 and 5 ppm, respectively (Montero and Bea, 1998), and typical detection limits are considered to be below 10% of chondritic values. Representative analyses of international standards analyzed in the Granada laboratory are shown in Table 1 and were also reported by Torres-Ruiz et al. (2003).

Sr and Nd isotope composition was determined by TIMS (thermal ionization mass spectrometry) at the CIC-UGR in a Finnigan Mat 262, following ultraclean acid digestion of the samples and chromatographic separation with ion-exchange resins. Normalization values were $^{86}Sr/^{88}Sr = 0.1194$ and $^{146}Nd/^{144}Nd = 0.7219$. The external precision (2σ), estimated by analyzing 10 replicates of the standard WS-E

Table 1
Major (%, by XRF-fused beads) and trace elements (ppm, by ICP-MS, except Zr by XRF) for Socovos Fault and Moratalla-Cehegin lamproites.

	Socovos Fault lamproites (W-E sorted)											Moratalla-Cehegin		PM-S	PM-S
Sample	09LA-12	09LA-7	09LA-11	09LA-10	DC-06	09LA-8	09-LA-9	08LA-9	08LA-14D	DC-22	DC-24	PU-1	TA-6	Analyzed	Certified
Dike name	DC-03	DC-04	DC-CN	DC-13	DC-06	DC-13	DC-16	DC-17	DC-18	DC-22	DC-24	DC-CPU	DC-CTA		
Position (W–E)	1	2	3	4	5	7	8	9	10	11	12				
Latitude (N)	38°15.6′	38°14.8′	38°14.5′	38°14.1′	38°13.9′	38°13.6′	38°13.6′	38°12.9′	38°13.3′	38°13.2′	38°12.8′	38°08.5′	38°09.1′		
Longitude (W)	1°48.0′	1°45.0′	1°43.1′	1°42.6′	1°41.8′	1°40.4′	1°40.2′	1°37.6′	1°37.0′	1°35.7′	1°34.7′	1°48.0′	1°49.3′		
SiO_2	57.0	55.4	56.2	56.6	57.0	59.8	55.0	54.6	57.1	56.0	54.6	55.5	55.5		
TiO_2	1.78	1.71	1.64	1.73	1.68	1.64	1.67	1.55	1.67	1.62	1.41	1.68	1.96		
Al_2O_3	9.9	10.6	9.5	9.9	9.8	9.7	10.4	8.4	9.8	9.6	8.6	8.3	9.8		
Fe_2O_3	4.8	5.5	5.3	5.1	5.0	4.2	5.7	5.0	5.2	5.3	4.9	5.6	5.5		
MnO	0.05	0.06	0.07	0.05	0.06	0.06	0.07	0.07	0.06	0.05	0.07	0.04	0.04		
MgO	10.7	8.8	12.0	9.2	10.6	4.8	6.8	12.1	11.0	11.3	12.5	13.3	9.9		
CaO	2.84	3.56	2.69	3.49	2.91	5.4	5.7	3.62	3.06	2.06	3.61	3.50	4.66		
Na_2O	0.31	0.47	0.22	0.65	0.66	0.60	0.39	0.95	1.96	0.61	1.60	0.78	0.47		
K_2O	8.9	10.2	9.9	9.3	10.0	9.7	9.8	9.0	6.7	9.6	8.8	8.0	9.3		
P_2O_5	1.18	1.43	1.12	1.08	0.96	0.93	1.57	1.52	1.03	1.15	1.34	1.13	0.97		
LOI	2.28	1.69	0.87	1.99	0.63	2.52	2.32	2.45	1.75	2.07	1.93	2.09	1.87		
Sum	99.62	99.41	99.51	99.07	99.20	99.28	99.26	99.23	99.37	99.23	99.25				
Mg#	0.82	0.76	0.82	0.78	0.81	0.70	0.70	0.83	0.81	0.81	0.84	0.82	0.78		
Li	45	56	43	78	64	34	77	77	49	108	58	65	57	7.5	*7.3*
Be	23.1	25.5	20.6	21.7	14.8	21.4	22.5	20.2	18.5	16.3	16.3	19.8	25.1	0.47	*0.5*
Rb	697	852	737	432	866	726	614	643	360	614	510	300	480	1.02	*1*
Cs	45	14.2	44	8.6	18.2	15.8	12.1	10.3	9.9	12.0	15.3			0.39	*0.35*
Sr	870	640	558	745	739	515	1675	1685	496	838	1391	680	584	277	*280*
Ba	2539	1927	1883	2047	1276	1518	2669	2576	1287	3276	3892	2402	1881	148	*148*
Sc	12.0	12.8	12.3	12.9	16.0	12.9	11.3	11.5	13.1	16.6	17.3	14.8	15.4	34	*34*
V	83	95	88	93	110	101	73	71	82	103	89	84	93	194	*192*
Cr	477	442	434	396	866	511	658	669	560	831	1426	446	536	266	*280*
Co	29.7	28.8	35	30	35	24.2	30	29.4	31	35	42	41	41	48	*49*
Ni	505	365	470	424	849	148	416	411	442	611	856	633	563	119	*115*
Cu	34	37	33	29.9	40	36	22.3	22.9	9.6	28.9	37	28.1	33	56	*59*
Zn	100	100	88	91	101	98	99	94	70	94	72	104	101	59	*60*
Ga	23.1	23.1	21.7	25.9	32	22.7	20.6	22.5	24.6	29.4	26.2	9.6	14.7	15.2	*16*
Y	28.0	23.8	24.3	26.1	30.4	23.5	24.7	26.2	28.1	34	37	22.6	23.6	10.7	*11*
Nb	49	47	41	48	53	47	57	59	50	66	89	48	48	2.29	*2.6*
Ta	3.8	3.2	3.1	3.8	4.6	3.3	3.9	4.2	3.9	5.1	7.1	6.3		0.20	*0.18*
Zr	969	869	849	905	874	849	907	848	905	991	1013	773	883	38	*39*
Hf	27.3	24.3	23.6	66	38	23.7	24.7	57	63	41	46	23.9	27.1	1.08	*1.12*
Mo	0.79	0.61	0.70	1.54	0.48	0.42	0.12	0.56	2.88	0.61	0.63	0.20	0.15	1.78	*1.9*
Sn	28.1	21.7	24.3	22.0	18.3	21.4	27.4	22.4	19.5	21.1	24.6	19.8	18.8	1.28	*3*
Tl	1.97	3.68	1.48	1.19	0.69	2.47	2.10	1.92	0.84	2.02	1.77	5.2	3.21	0.04	*0.04*
Pb	114	70	71	76	73	83	21.1	20.0	17.6	7.5	78	93	52	1.21	*2.5*
U	24.0	9.4	26.3	28.4	16.7	28.3	33	38	36	34	51	31	12.2	0.01	*0.03*
Th	128	130	108	127	140	124	138	146	124	177	220	116	137	0.05	*0.05*
La	117	96	95	100	114	121	113	105	90	111	112	85	112	2.8	*2.8*
Ce	319	265	263	278	335	334	294	273	250	318	305	232	310	7.7	*6.8*
Pr	46	39	39	42	58	48	43	40	38	55	50	36	47	1.12	*1.08*
Nd	203	175	173	161	250	206	187	185	152	239	217	165	208	5.9	*5.5*
Sm	38	33	33	27.9	44	36	35	36	27.2	43	41	32	38	1.77	*1.75*
Eu	6.6	5.3	5.2	4.9	6.3	5.3	5.8	4.8	4.9	6.4	6.3	5.3	6.2	1.12	*1.07*
Gd	21.8	18.7	18.4	15.9	21.3	19.8	19.4	15.6	15.5	21.4	21.0	20.2	23.9	1.93	*2*
Tb	2.38	2.17	2.12	1.78	2.33	2.26	2.18	1.77	1.76	2.33	2.43	1.87	2.14	0.32	*0.36*
Dy	8.8	7.5	7.4	6.2	7.3	8.0	7.4	6.2	6.4	7.7	8.6	6.7	7.4	2.06	*2*
Ho	1.12	0.97	1.02	0.97	1.15	1.00	0.99	0.94	1.04	1.22	1.29	0.86	0.92	0.44	*0.42*
Er	2.16	2.01	1.92	2.04	2.40	2.08	2.02	1.91	2.32	2.69	2.78	2.64	3.00	1.12	*1.1*
Tm	0.31	0.27	0.28	0.28	0.34	0.30	0.25	0.26	0.32	0.38	0.38	0.24	0.25	0.17	*0.17*
Yb	1.96	1.65	1.84	1.60	2.08	2.00	1.74	1.52	1.88	2.36	2.28	1.64	1.69	1.01	*1*
Lu	0.27	0.27	0.29	0.24	0.29	0.26	0.24	0.23	0.29	0.35	0.33	0.20	0.21	0.16	*0.15*

(Govindaraju et al., 1994), was better than ± 0.003% for $^{87}Sr/^{86}Sr$ and ± 0.0015% for $^{143}Nd/^{144}Nd$ (Bea et al., 2003). $^{87}Rb/^{86}Sr$ and $^{147}Sm/^{144}Nd$ were directly determined by ICP-MS following the method developed by Montero and Bea (1998) with a precision better than ± 1.2% and ± 0.9% 2σ, respectively.

A preliminary survey of mineral compositions was carried out with a Cameca SX100 electron probe micro analyzer (EPMA) at the University of Granada, equipped with four wavelength dispersive spectrometers, using both natural and synthetic standards. An accelerating voltage of 20 kV, with a beam current of 30 nA and a beam diameter of ~ 2 μm, was used. Counting times on peaks were twice those of backgrounds, with 15 s for Na and K; 20 s for Ti and Ca; 25 s for Fe, Si and Al; and 30 s for Mg. Na was counted first in order to minimize Na mobility during analysis. Data were reduced using the procedure of Pouchou and Pichoir (1985).

3.2. $^{40}Ar/^{39}Ar$ geochronology

Eight lamproite samples from the Socovos Fault and Moratalla-Cehegín area (Fig. 2) were dated by laser $^{40}Ar/^{39}Ar$ incremental heating. Following a petrographic investigation, we selected relatively unaltered samples, six from the Socovos Fault zone and two additional samples from outside the fault zone. The analyses were performed on whole-rock for samples DC-CTA and DC-CN and on phlogopite grains for the rest of the samples.

Samples were crushed to 1–2 mm, washed in absolute ethanol and then air-dried. We analyzed 4 whole-rock grains from each sample DC-CTA and DC-CN and 12–19 phlogopite grains from each sample DC-04, DC-21, DC-17, DC-CM2, DC-27 and 08LA-2. Grains were loaded into a 21-pit Al disk along with the neutron fluence Fish Canyon monitor (28.201 ± 0.046 Ma, Kuiper et al., 2008), following the geometry described by Vasconcelos et al. (2002). The disks were closed with aluminum cover, wrapped in aluminum foil, vacuum heat sealed into quartz vials and irradiated for 14 h over the period from 18 July 2012 to 23 July 2012 for samples DC-27 and 08LA-2 and from 25 January 2011 to 26 January 2011 for the rest of samples. Irradiation was done in the Cadmium-lined B-1 CLICIT facility, a TRIGA-type reactor, Oregon State University. After a post-irradiation decay period, the samples were separately analyzed by the laser step heating $^{40}Ar/^{39}Ar$ method at the University of Queensland Argon Geochronology Earth Sciences (UQ-AGES) laboratory. Before analysis, the rock grains and fluence monitor were baked-out under vacuum at ~200 °C for ca. 12 h. Each grain was heated incrementally with a continuous-wave Ar-ion laser with a 2 mm wide defocused beam. The gasses released during laser heating were cleaned by a cold trap (−133 °C) and two C–50 SAES Zr–V–Fe getters, and analyzed in a MAP 215-50 noble gas mass spectrometer. Full system blanks and air pipettes were determined before and after each sample. The resulting data were corrected for nucleogenic interferences, atmospheric contamination and mass discrimination following the procedures in Vasconcelos et al. (2002), using the software "MassSpec Version 7.527" developed by Alan Deino of the Berkeley Geochronology Centre. J-factors for each Al-disk were determined by the laser total fusion analyses of 15 individual aliquots of neutron fluence monitor, each consisting of one to three grains of Fish Canyon sanidine. An $^{40}Ar/^{36}Ar$ value of 298.56 ± 0.31 for atmospheric argon was used for the calculation of the mass spectrometer discrimination (Lee et al., 2006).

$^{40}Ar/^{39}Ar$ ages were calculated using the following accepted decay constants (Steiger and Jäger, 1977): ^{40}K isotopic abundance: 0.01167; ^{40}K epsilon: $(0.581 \pm 0.017) \times 10^{-10}$ yr^{-1}; ^{40}K beta: $(4.962 \pm 0.086) \times 10^{-10}$ yr^{-1}; ^{37}Ar decay: 0.01975 d^{-1}; ^{39}Ar decay: 7.068×10^{-6} d^{-1}; ^{36}Cl decay: 6.308×10^{-9} d^{-1}. Errors are quoted at the 2σ confidence level (95%), including the errors in J and the errors in the irradiation correction factors. The tabulated data from the analyses (Table A1), as well as $^{40}Ar/^{39}Ar$ plateau and probability ages are presented in Appendix A.

4. Results

4.1. Petrography and mineral chemistry

The studied rocks are defined as olivine phlogopite lamproites, using the nomenclature of Mitchell and Bergman (1991). The rocks are microporphyritic with phlogopite, olivine, diopside, apatite and ore microphenocrysts in a glassy to microcrystalline groundmass, partially recrystallized to K-feldspar. The rocks are scarcely vesicular or non-vesicular, and commonly include abundant host rock sedimentary-derived xenoliths. Most samples show pervasive alteration to clay minerals and mixing with secondary carbonate minerals.

Phlogopite phenocrysts commonly appear as abundant euhedral to subhedral mm-sized plates, mainly composed of zoned yellowish-whitish cores and slightly darker rims. A preliminary EPMA survey shows high and homogeneous values of magnesian composition from cores (Mg# 0.93–0.94, Al_2O_3: 11.1–11.6%, TiO_2: 1.5–2.2%) to rims (Mg# around 0.92). There are also smaller, unzoned subhedral phlogopite crystals in the groundmass. Some anhedral varieties with more ferrous-titanian composition (Mg# 0.85, Al_2O_3: 9.8%, TiO_2: 6.4%) resemble partially resorbed xenocrysts. These compositions also occur as partially resorbed, patchy cores inside larger euhedral phlogopites (Fig. 3A).

Olivine is less abundant than phlogopite and usually strongly altered. In the freshest samples, we have recognized two olivine varieties. The first type corresponds to anhedral crystals or aggregates (2–4 mm), with very irregular, serrated boundaries, undulose extinction and kink-bands (Fig. 3B), pointing to a xenocrystic origin (Fo_{91}). The other variety of olivine is smaller (0.1–0.3 mm) subhedral to euhedral grains that show engulfments (Fo_{92-94}). Some of the phenocrysts contain small chromite inclusions (~58% Cr_2O_3, ~2.5% TiO_2).

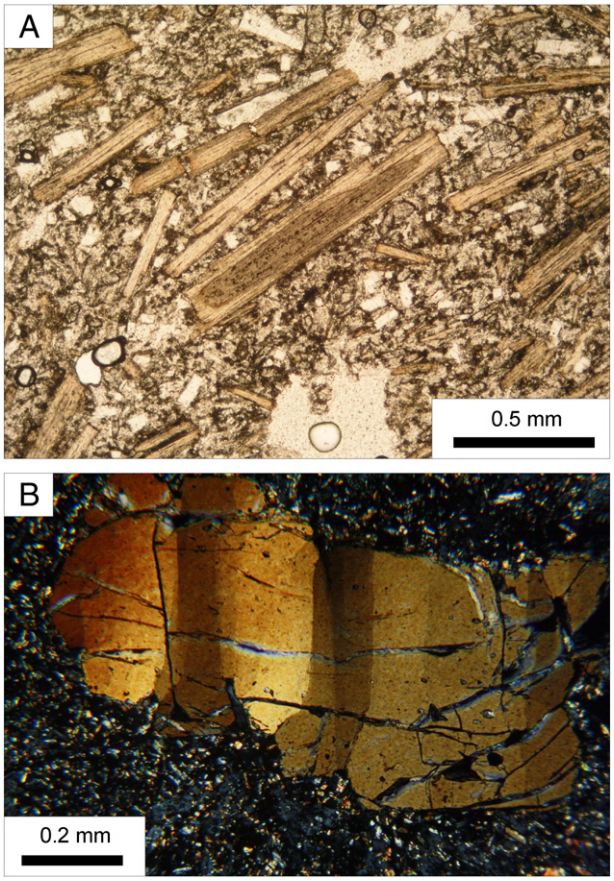

Fig. 3. A) Microphotograph showing a phlogopite grain with a ferrous-titanian xenocrystic core. B) Microphotograph showing an olivine xenocryst.

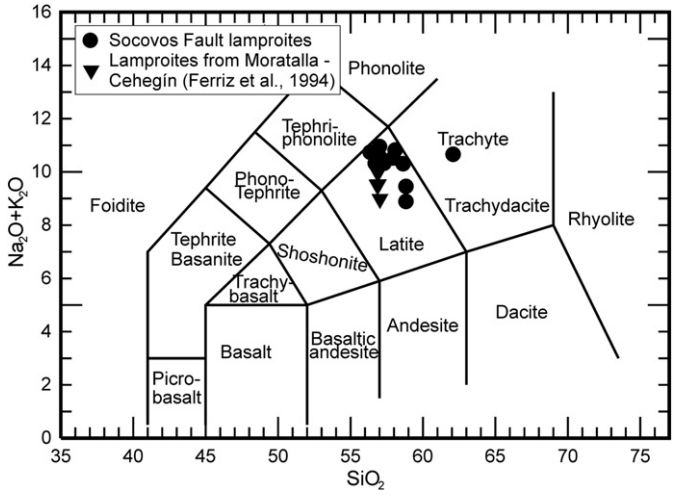

Fig. 4. Silica vs. total alkali diagram (TAS, Le Bas et al., 1986) showing a comparison of the Socovos Fault lamproites with lamproite dikes from Moratalla-Cehegín (triangles).

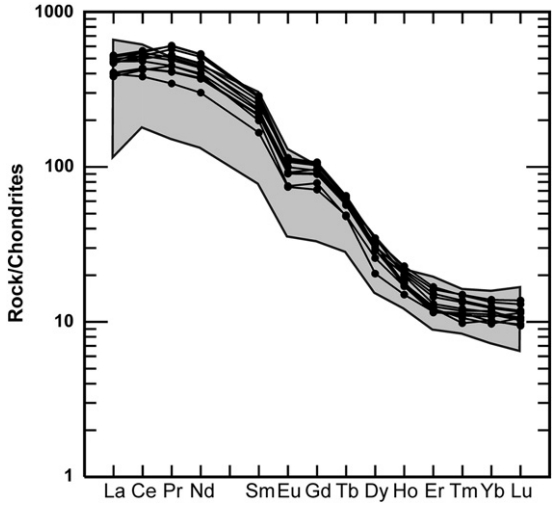

Fig. 6. Diagram of REE normalized to the chondritic values of Sun and McDonough (1989). The shaded field corresponds to lamproitic rocks from SE Spain (Conticelli et al., 2009; Duggen et al., 2005; Prelević et al., 2008; Turner et al., 1999; Venturelli et al., 1984).

In some of the samples, we found scarce subhedral diopside microphenocrysts (≈0.1 mm). Diopside is also abundant in the groundmass, as subhedral to euhedral prisms. Its composition is $En_{45-50}Fs_6Wo_{43-49}$, with significant contents of TiO_2 and Cr_2O_3 (0.5–1%).

The groundmass (>60%) is composed of microcrystalline diopside, phlogopite flakes, apatite needles, anhedral potassium feldspar, scarce opaque minerals and interstitial glass. Other glassy-rich varieties are also present. Scarce analcitized leucite was found in samples from Moratalla-Cehegín lamproites (Férriz et al., 1994).

4.2. Major and trace elements

Major and trace elements of the lamproite dikes intruded along the Socovos Fault and in the nearby Moratalla-Cehegín area are presented in Table 1. Due to pervasive alteration and contamination with carbonate, only analyses with less than 4% LOI (loss on ignition) have been used. Major element composition is similar to other ultrapotassic rocks from the SE Spain Volcanic Province (e.g., Conticelli et al., 2009; Duggen et al., 2005; Fúster et al., 1967; Prelević et al., 2008; Venturelli et al., 1984). The rocks are ultrapotassic (MgO > 3%, K_2O > 3%, and K_2O/Na_2O > 2), with moderate SiO_2 values (54–57.1%), high MgO (4.8–12.2%), K_2O (6.7–10.2%), and P_2O_5 (0.9–1.5%), and very low Al_2O_3 (8.4–10.6%) and Na_2O (0.2–1.9%) (Fig. 4). K_2O values are among the highest recorded in the SE Spain Volcanic Province, and Mg# values are very high (0.70–0.84). We have not found any clear correlation trend among major element contents.

The variation in compatible trace element contents is large, from moderate to very high (Ni: 148 to 856 ppm, and Cr: 430–1425 ppm), and unrelated to the SiO_2 or MgO contents. Incompatible trace element contents are displayed in Fig. 5 as multielemental diagrams normalized to the primitive mantle values of Sun and McDonough (1989). Reference values for OIB and MORB basalts are also shown, as well as the field for published analyses of lamproites from the SE Spain Volcanic Province (Conticelli et al., 2009; Duggen et al., 2005; Prelević et al., 2008; Turner et al., 1999; Venturelli et al., 1984). The diagram shows enrichment in Cs, Rb, K, Th, U, and Pb, and relatively lower values for Ba and some high-field-strength elements (HFSE: Ti, Nb, Ta, heavy REE). Zr, Sr (and P) show values higher than OIB but with lower values than adjacent elements. Evidence for a crustal component involved in the origin of lamproites is indicated by high LILE (large ion lithophile elements) and LREE contents, high LILE/HFSE ratios, troughs at Nb and Ta, and a Pb peak (Fig. 5).

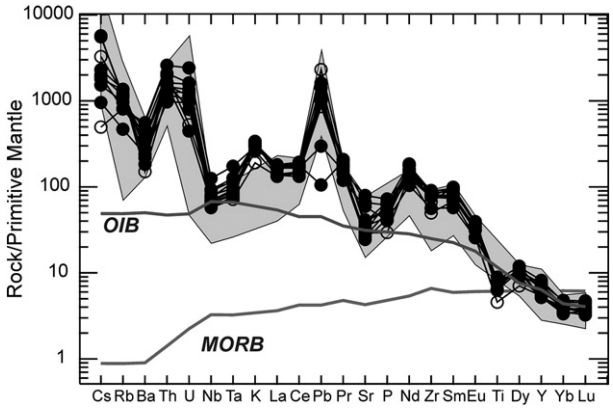

Fig. 5. Spider diagram for the studied lamproites normalized relative to a primitive mantle (Sun and McDonough, 1989). The OIB and MORB values are from Sun and McDonough (1989). The shaded field corresponds to other lamproitic rocks from SE Spain (Conticelli et al., 2009; Duggen et al., 2005; Prelević et al., 2008; Turner et al., 1999; Venturelli et al., 1984).

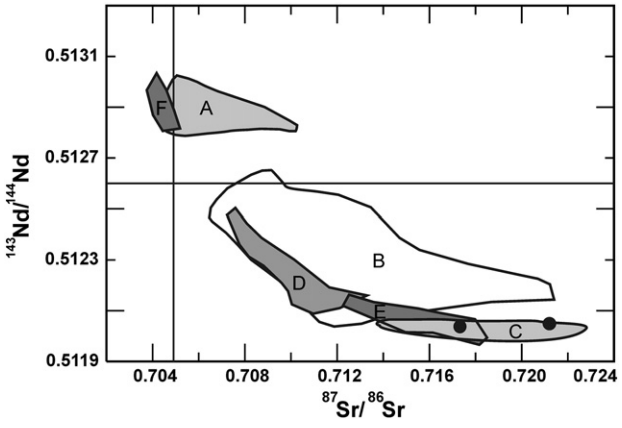

Fig. 7. Nd–Sr isotope diagram showing a comparison between the Socovos Fault lamproites and other volcanic rocks from the Alborán, the Neogene Volcanic Province of SE Spain and Mediterranean lamproites. Fields are: (A) Depleted, tholeitic to calc-alkaline basalts and andesites from Alborán and Málaga; (B) Calc-alkaline, K-rich calc-alkaline and shoshonitic volcanic series from SE Spain; (C) Lamproites from SE Spain; (D) Serbian lamproites; (E) Italian lamproites; (F) Tallante alkali basalts. Data from Duggen et al., 2004; Duggen et al., 2005; Turner et al., 1999; Prelević et al., 2008; Conticelli et al., 2009 and our unpublished data.

Table 2
Rb, Sr, Sm, Nd concentration (ppm) and isotopic data (by ICP-MS and TIMS).

Socovos fault lamproites													
Sample	Rb (ppm)	Sr (ppm)	$^{87}Rb/^{86}Sr$	$^{87}Sr/^{86}Sr$	Error Sr/Sr	$^{87}Sr/^{86}Sri$	Sm (ppm)	Nd (ppm)	$^{147}Sm/^{144}Nd$	$^{143}Nd/^{144}Nd$	$^{143}Nd/^{144}Ndi$	Error Nd/Nd	ε Nd (8 Ma)
09LA-11	640	495	3.748	0.72116	0.003	0.72074	31	158	0.118	0.51205	0.51205	0.002	−11.35
09LA-12	582	748	2.252	0.71735	0.003	0.71709	36	187	0.116	0.51204	0.51203	0.002	−11.62

The Rare Earth Element (REE) patterns are fractionated with an extreme enrichment in light REE, and a small negative Eu anomaly (Eu/Eu*: 0.61–0.7) (Fig. 6, normalized to the chondritic values of Sun and McDonough, 1989). These REE patterns are similar to the patterns described for other lamproites in SE Spain and the Mediterranean (e.g., Conticelli et al., 2009; Duggen et al., 2005; Prelević et al., 2008; Turner et al., 1999).

We have found irregular variations in dike chemical composition along the Socovos Fault. From W to E, there is a decrease in TiO_2, Pb, and an increase in Na_2O, Ba, Cr, Nb, Th, and U. Other elements show irregular variations (MgO and CaO increase from west to east, except for two central samples). The remaining elements show no trend along the fault.

4.3. Sr and Nd isotopes

The samples analyzed are characterized by high and variable values of $^{87}Sr/^{86}Sr$ (0.71735–0.72116) and relatively uniform low $^{143}Nd/^{144}Nd$ ratios (0.51204–0.51205) (Fig. 7 and Table 2). The latter correspond to negative initial ε_{Nd} values of (−11.35) − (−11.62), corrected for an age of 8 Ma. The samples plot in the enriched quadrant of the Sr–Nd isotope diagram (Fig. 7). Our samples are within the field of other lamproites from SE Spain (e.g., Conticelli et al., 2009; Prelević et al., 2008; Turner et al., 1999), but Nd isotopic ratios are lower than those reported by Duggen et al. (2005).

4.4. $^{40}Ar/^{39}Ar$ geochronological data

Geochronological results are presented as isochron ages (Fig. 8). The distribution of ages along the Socovos Fault (Fig. 2) show older ages for eastern samples (east of Calasparra) DC-21 (8.2 ± 0.2 Ma), DC-17 (9.3 ± 0.2 Ma) and DC-27 (9.0 ± 0.1 Ma; 8.2 ± 0.1 Ma); and younger ages for western samples (west of Calasparra) DC-CN (7.1 ± 0.1 Ma) DC-04 (7.2 ± 0.2 Ma) and 08LA-02 (7.3 ± 0.2 Ma). The ages indicate a ~2 Ma period of lamproitic volcanism along the ~25 km segment of the Socovos Fault. Outside the fault zone, the two dated samples have yielded ages of 7.5 ± 0.1 Ma south of the fault (DC-CTA) and 6.9 ± 0.2 Ma north of the fault (DC-CM2). All duplicate grains show compatible ages within the 2σ error, except of sample DC-27, from the easternmost dike, which shows two different ages for the two grains, 9.0 ± 0.1 Ma and 8.2 ± 0.1 Ma.

5. Discussion

5.1. Age of lamproitic magmatism

Based on the closure temperature estimated for Argon in the biotite/phlogopite system (~450 °C, e.g., Reiners and Brandon, 2006) and the estimated temperature of crystallization for lamproite minerals (1200 °C to 650 °C, Salvioli-Mariani and Venturelli, 1996), we consider the $^{40}Ar/^{39}Ar$ ages as emplacement ages. In some kimberlite systems, the phlogopite ages do not represent emplacement ages due to the

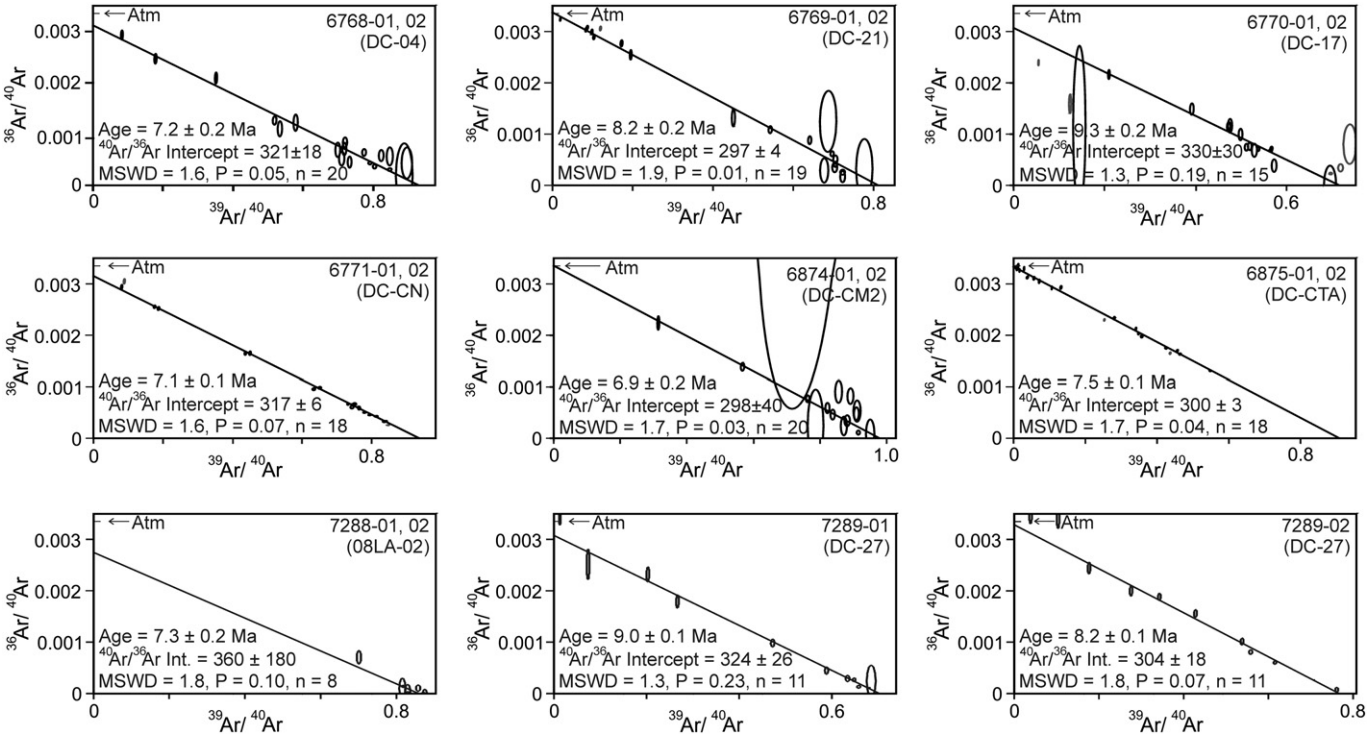

Fig. 8. $^{40}Ar/^{39}Ar$ vs. $^{36}Ar/^{40}Ar$ isotope correlation diagrams (inverse isochrones) for incremental heating of duplicate grains from each sample and individual grains from DC-27 (see incremental heating data and diagrams for each grain in supplementary data). The diagrams show isochron ages compatible at the 2σ confidence level with plateau ages, except of DC-CN that yielded a younger age. $^{36}Ar/^{40}Ar$ intercepts for all samples except DC-CN are within error of the present atmospheric (Atm) value of 298.56. The inverse isochron ages permit obviating the effects of small quantities of excess Ar, possibly present in sample DC-CN.

rapid ascent and low diffusion rate of Ar in phlogopite (e.g., Hopp et al., 2008; Kelley and Wartho, 2000). In these cases, phlogopite grains are mainly derived from mantle xenoliths and show an increasing age pattern on incremental step heating analysis (Hopp et al., 2008). The phlogopites dated here are phenocrysts with euhedral or subhedral shape, indicating that they were probably generated in a single crystallization event. Moreover, the incremental step heating analysis of all phlogopite grains yielded almost flat spectra, with almost no evidence for a stepwise increase in ages (see $^{39}Ar/^{40}Ar$ plateau diagrams, Appendix A). Therefore, the various plateau ages obtained in the different samples are interpreted as different emplacement ages of the lamproite dikes.

The only $^{40}Ar/^{39}Ar$ age that is somewhat more complicated is from sample DC-27, which yielded two different ages for the two dated phlogopite grains. This sample corresponds to one of the thickest and longest dike, which also includes granitic xenoliths and phlogopites with a ferrous-titanian rich xenocrystic core. These different ages could be explained if one of the phlogopites has a xenocrystic core, in which the Ar system had not been reset. However, a stepwise pattern during incremental heating is expected if the dated phlogopites are indeed characterized by xenocrystic cores. The two dated phlogopites have similar size and thickness, and both resulted in flat spectra (Fig. 9), thus excluding the possibility for a partial Argon diffusive loss. Excess Argon does not appear to be present, or at least is not detectable for the older grain within the error margin. We therefore think that the ages of the two phlogopite grains are emplacement ages, with the older grain possibly representing a phlogopite from an older dike emplaced into an upper crustal level at ~9.0 Ma and reassimilated by a new dike intrusion at ~8.2 Ma. This process occurred without sufficient time to reset the system, thus resulting in an older age for the reassimilated grain. The possibility that different generations of melts followed a similar pathway during ascent is consistent with our suggestion that the Socovos Fault acted as a channel for lamproite melts (see Section 5.3). Evidence for older dikes in the proximity of sample DC-27 is found in sample DC-17, which yielded an age of 9.3 Ma.

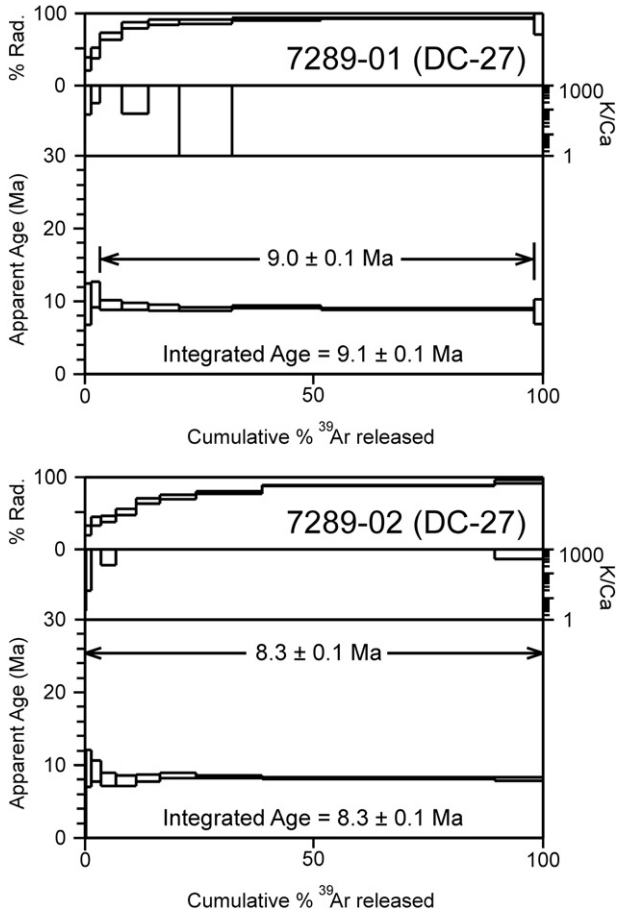

Fig. 9. Incremental step-heating data for both grains of phlogopite from sample DC-27.

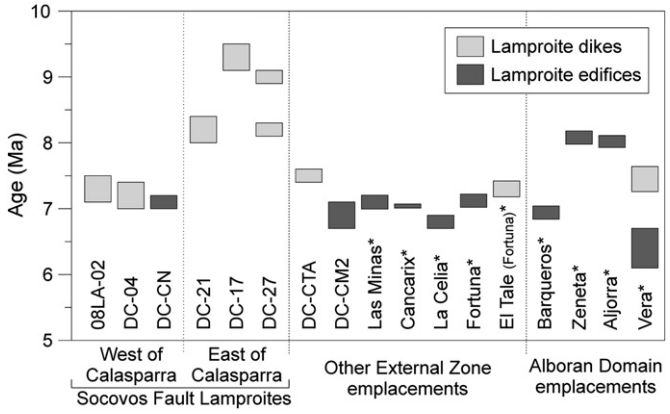

Fig. 10. Age distribution of lamproites from the SE Spain Neogene Volcanic Province. *Data from Duggen et al. (2005).

The ages of lamproite dikes emplaced within the South-Iberian paleomargin range from 9.3 to 7.2 Ma, whereas lamproite edifices range from 7.1 to 6.8 Ma (Fig. 10, our data and Duggen et al., 2005). This shows that the dikes are generally older than volcanic edifices, though we note that the ages (with errors) of the youngest dikes and the older lamproite edifices overlap. For the lamproites emplaced along the Socovos Fault, the $^{40}Ar/^{39}Ar$ ages show an age zonation characterized by older ages in the eastern zone and younger ages in the western zone (Fig. 10). This pattern suggests that lamproitic volcanism generally migrated along the fault westward. Within the Alborán Domain, lamproites range from 8 to 6.4 Ma (Fig. 10) (Duggen et al., 2005). Nevertheless, some of the latter lamproites recorded a process of magma mixing involving crustal melts (Zeneta, Toscani et al., 1995; Zeneta and Aljorra, Cambeses, 2011) originated beneath the Alborán Domain at ~9 Ma (Cesare and Gómez-Pugnaire, 2001) indicating that these lamproites may have experienced different ascent patterns than those emplaced within the South-Iberian paleomargin.

5.2. Petrogenesis of the lamproites

The origin of Mediterranean lamproites is a matter of debate, but it is generally agreed that the source of these melts is within an ultra-depleted mantle contaminated by subduction-related crustal material (Benito et al., 1999; Conticelli et al., 2009; Peccerillo and Martinotti, 2006; Prelević and Foley, 2007; Prelević et al., 2007; Turner et al., 1999). In our samples, we have found a similar geochemical signature, with high Mg, Ni and Cr content, and high-Mg olivine phenocrysts (up to Mg#-0.94), pointing to an ultra-depleted mantle source (e.g., Prelević and Foley, 2007). Furthermore, our samples show enrichment in incompatible elements (high LILE and LREE contents, high LILE/HFSE ratios, troughs at Ba, Nb, Ta, Sr and P, and a peak at Pb), which is characteristic of a crustal component derived from sediments recycled within the subcontinental lithospheric mantle (SCLM). This evidence highlights the importance of subduction processes in the genesis of the metasomatized SCLM where the Mediterranean lamproites were sourced (e.g., Nelson, 1992; Peccerillo and Martinotti, 2006; Prelević et al., 2008). We emphasize, however, that the petrogenesis of the lamproites was likely more complex, as indicated by the abundance of several elements and their relationships (e.g., Th/La, Sm/La and isotope composition of Pb, Sr and Nd) that cannot be explained by the simple model of an ultra-depleted SCLM metasomatized by slab derived sediments (Prelević et al., 2008; Tommasini et al., 2011).

The majority of lamproites from the SE Spain Neogene Volcanic Province occur in the South-Iberian paleomargin (Fig. 1), relatively

close to the Iberian foreland. Orogenic deformation within the South-Iberian paleomargin started in the Early Miocene, but there is no evidence that subduction processes affected the underlying lithosphere of Gibraltar Arc Miocene subduction during the Mesozoic and Cenozoic (Platt et al., 2013 and references therein). It is therefore unlikely that Miocene subduction processes were responsible for metasomatizing the Iberian SCLM, thus suggesting that this metasomatism may have occurred prior to the Mesozoic. This interpretation contrasts with other models (e.g., Murphy et al., 2002; Prelević et al., 2008), which assumed, based on Pb isotopic compositions in lamproites, that metasomatism of the Iberian SCLM was predominantly controlled by a recent subduction. However, Tommasini et al. (2011) pointed out that the measured Pb isotopic compositions require a long-term (>100 Ma) isolation, having been generated earlier.

To sum up, we suggest that SE Spain lamproite petrogenesis involved a Pre-Mesozoic stage responsible for their characteristic geochemical signature, followed by a second stage of mantle partial melting, triggered by Late Miocene crustal extension (see Section 5.3). This petrogenetic model is somewhat similar to the one described by Tommasini et al. (2011) for Tethyan lamproites, with the difference that in SE Spain, mantle metasomatism was not driven by recent subduction.

5.3. Geodynamic implications

Geodynamic scenarios proposed for the formation of the Betic-Rif orogen can be grouped into two main models: (1) subduction rollback and slab tearing (e.g., Gutscher et al., 2012; Lonergan and White, 1997; Rosenbaum and Lister, 2004); and (2) continental delamination and/or convective removal of an overthickened continental lithosphere (e.g., Booth-Rea et al., 2007; Calvert et al., 2000; Duggen et al., 2005; Platt et al., 2003b). The convective removal/delamination model mainly assumes vertical movements, and predicts a radial distribution of deformation at the upper crust. In contrast, the subduction rollback model assumes large lateral movements, propagating westward. Most geophysical data, namely seismic tomography (Spakman and Wortel, 2004), SKS splitting (Bokelmann et al., 2011; Buontempo et al., 2008; Díaz et al., 2010) and GPS data (Nocquet, 2012; Palano et al., 2013), are consistent with the subduction rollback model. Volcanic rocks of the CA-KCA-SH series were emplaced in the Alborán Domain, in a supra-subduction environment (e.g., Duggen et al., 2005). Therefore, the geochemistry of volcanic rocks is also compatible with subduction rollback (e.g., Duggen et al., 2008), except for some of the ultrapotassic rocks that were emplaced outside the supra-subduction zone.

The emplacement of lamproites occurred ubiquitously both in the Alborán Domain and the South-Iberian paleomargin, with most occurrences in the South-Iberian paleomargin. As pointed out earlier (see Section 5.2), there is no evidence for Neogene subduction underneath the South-Iberian paleomargin, thus implying that a supra-subduction origin for the lamproites is unlikely. Therefore, partial melting responsible for the origin of lamproites was likely generated in the underlying mantle lithosphere of the Betic orogen (i.e. Iberian lithosphere), possibly triggered by decompressional melting due to Late Miocene crustal extension (e.g., Booth-Rea et al., 2007). Decompressional melting could have resulted in the very low melt rates invoked for lamproite melt formation (<1%, e.g., Benito et al., 1999). This stage of crustal extension may have also resulted in crustal melting beneath the Alborán Domain (Cesare and Gómez-Pugnaire, 2001), as indicated by the geochemical features of crustal xenoliths from volcanic rocks of the KCA and SH series (Álvarez-Valero and Kriegsman, 2007, 2008; Cesare and Gómez-Pugnaire, 2001; Cesare et al., 2008). The existence of present-day crustal melting beneath the Alborán Domain (Soto et al., 2008) may also explain the low velocity zones observed in seismic images (e.g., Julià et al., 2005).

Lamproite occurrences along the Neogene Volcanic Province of SE Spain mostly correspond to relatively large isolated volcanic edifices with volcanic cones, domes, necks, plugs, maars and lava flows (e.g., Seghedi et al., 2007). In contrast, lamproitic dikes were relatively rare, with only four known occurrences outside the Socovos Fault zone (Moratalla-Cehegín, Mula, Fortuna and Vera). The occurrence of

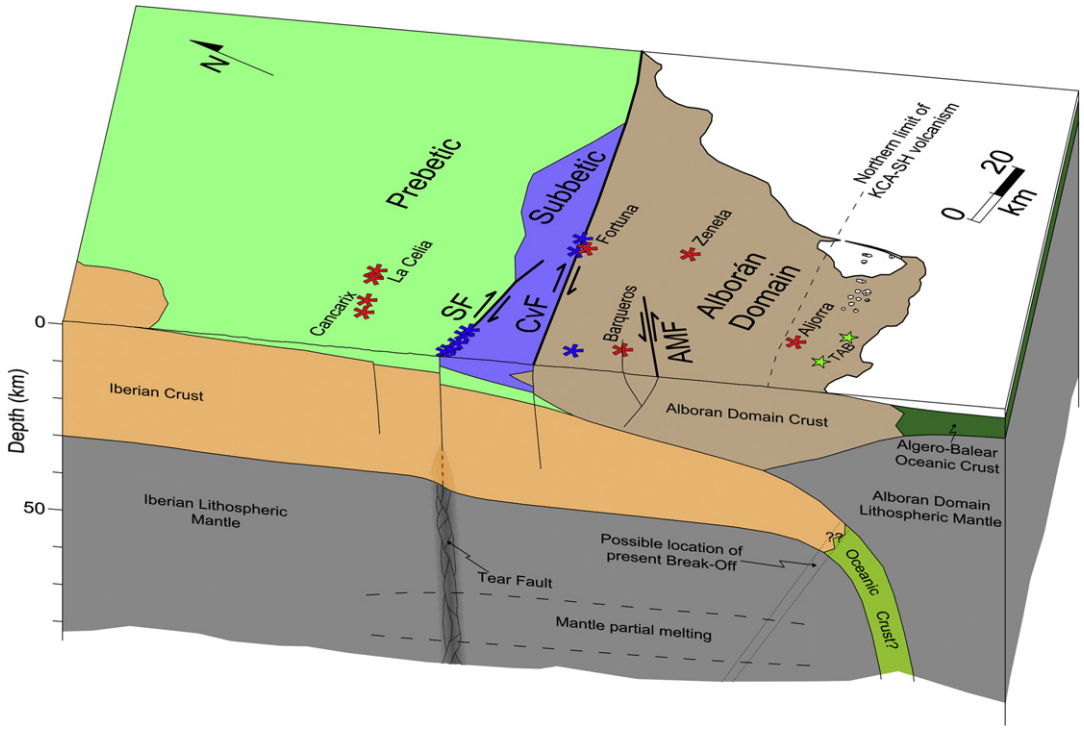

Fig. 11. Schematic illustration of the lithospheric structure in the eastern Betics, showing the ascent of lamproitic melt from its mantle source (Iberian lithospheric mantle). SF: Socovos Fault; CvF: Crevillente Fault; AMF: Alhama de Murcia Fault; TAB: Tallante Alkali Basalts. Data extrapolated from Banda et al. (1993), Galindo-Zaldívar et al. (1997), Garcia-Castellanos et al. (2002), Jabaloy-Sánchez et al. (2007), Ruiz-Constán et al. (2012), Mancilla et al. (2013).

a cluster of lamproitic dikes along the Socovos Fault raises the question on the relationships between lamproitic magmatism and faulting. A spatial link between K-rich mantle-derived magmatism and lithospheric-scale strike-slip faulting has been documented in a number of tectonic environments (Carlier et al., 2005; Dilek and Altunkaynak, 2009; Pe-Piper and Piper, 2007; Prelević et al., 2007; Vaughan and Scarrow, 2003), but in all of these localities magmatism was not localized exactly within the fault zone. We do not claim that magmatism was triggered by faulting, but we propose that the Socovos Fault channelized the mantle-derived magmas through the upper crust, while a tear fault beneath the Socovos Fault channelized these magmas at depth, possibly across the upper lithospheric mantle and lower crust (Fig. 11). As such, the Socovos Fault may represent the upper crustal expression of a segment of a tear fault related to the northern edge of the Gibraltar subducted lithospheric slab that was rolling back westwards in the Late Miocene.

We propose that initiation of mantle melting processes beneath the Betics resulted in the intrusion of the oldest lamproite dikes at ~9 Ma, in agreement with the age of crustal anatexis beneath the Alborán Domain (Cesare and Gómez-Pugnaire, 2001). Tear faulting beneath the Socovos Fault area allowed the ascent of melts. We envisage that the volume of magma was very small and its ascent through the crust and upper lithospheric mantle was possible only through a mechanical pathway. The Socovos Fault and its related tear fault at depth may have acted as such a mechanical boundary during the ~2 Ma period from 9.3 Ma to 7.1 Ma. A change in the tectonic regime at ~7 Ma, from transpression to transtension (de Vicente et al., 2008; Galindo-Zaldívar et al., 1993; Martín-Velázquez et al., 1997), possibly led to the main phase of lamproitic magmatism, allowing the ascent of lamproitic melts through a broader network of pathways.

6. Conclusions

Intrusion ages of synkinematic lamproite dikes in the Socovos Fault range from 9.3 to 7.1 Ma. The unusual concentration of dikes along the fault suggests that the Socovos Fault is the upper crustal expression of a tear fault acting as a channel for the ascent of mantle-sourced lamproitic magmas through the upper crust. Partial melting in the Iberian SCLM commenced in the Late Miocene with a very low rate of melt production (<1%), giving rise to the older lamproitic dikes (9.3 to 8.2 Ma) in the eastern part of the Socovos Fault. The ascent of this melt was made possible by the mechanical discontinuity created by the tear fault in the lithospheric mantle and the Socovos Fault in the upper crust. The age distribution of dikes along the Socovos Fault is compatible with the westward retreat of the lithospheric slab. We therefore suggest that the Sovocos Fault represents the surface expression of a Late Miocene tear fault that accommodated a component of the required dextral kinematics at the northern edge of the retreating Gibraltar Arc.

Supplementary data to this article can be found online at http://dx.doi.org/10.1016/j.lithos.2013.08.016.

Acknowledgments

We thank two anonymous reviewers and Dejan Prelević for their constructive reviews, which have helped improving the quality of this manuscript. This work has been funded by the Spanish Ministry of Science and Innovation (MICINN) through the grants CONSOLIDER-INGENIO CSD-2006-00041 and CGL2006-10202/BTE, as well as by the Spanish Ministry of Education through a FPU grant to the first author (AP2008-03180).

References

Álvarez-Valero, A.M., Kriegsman, L.M., 2007. Crustal thinning and mafic underplating beneath the Neogene Volcanic Province (Betic Cordillera, SE Spain): evidence from crustal xenoliths. Terra Nova 19, 266–271.

Álvarez-Valero, A.M., Kriegsman, L.M., 2008. Partial crustal melting beneath the Betic Cordillera (SE Spain): the case study of Mar Menor volcanic suite. Lithos 101, 379–396.

Balanyá, J.C., Crespo-Blanc, A., Díaz-Azpiroz, M., Expósito, I., Torcal, F., Pérez-Peña, V., Booth-Rea, G., 2012. Arc-parallel vs back-arc extension in the Western Gibraltar arc: is the Gibraltar forearc still active? Geologica Acta 10, 249–263.

Banda, E., Gallart, J., García-Dueñas, V., Dañobeitia, J.J., Makris, J., 1993. Lateral variation of the crust in the Iberian peninsula: new evidence from the Betic Cordillera. Tectonophysics 221, 53–66.

Bea, F., Montero, P., Zinger, T., 2003. The nature, origin, and thermal influence of the granite source layer of Central Iberia. Journal of Geology 111, 579–595.

Beccaluva, L., Bianchini, G., Bonadiman, C., Siena, F., Vaccaro, C., 2004. Coexisting anorogenic and subduction-related metasomatism in mantle xenoliths from the Betic Cordillera (southern Spain). Lithos 75, 67–87.

Beccaluva, L., Bianchini, G., Natali, C., Siena, F., 2011. Geodynamic control on orogenic and anorogenic magmatic phases in Sardinia and Southern Spain: inferences for the Cenozoic evolution of the western Mediterranean. Lithos 123, 218–224.

Benito, R., López-Ruiz, J., Cebriá, J.M., Hertogen, J., Doblas, M., Oyarzun, R., Demaiffe, D., 1999. Sr and O isotope constraints on source and crustal contamination in the high-K calc-alkaline and shoshonitic neogene volcanic rocks of SE Spain. Lithos 46, 773–802.

Bokelmann, G., Maufroy, E., Buontempo, L., Morales, J., Barruol, G., 2011. Testing oceanic subduction and convective removal models for the Gibraltar arc: seismological constraints from dispersion and anisotropy. Tectonophysics 502, 28–37.

Booth-Rea, G., Ranero, C.R., Martínez-Martínez, J.M., Grevemeyer, I., 2007. Crustal types and Tertiary tectonic evolution of the Alborán sea, western Mediterranean. Geochemistry Geophysics Geosystems 8, Q10005. http://dx.doi.org/10.1029/2007GC001639.

Buontempo, L., Bokelmann, G.H.R., Barruol, G., Morales, J., 2008. Seismic anisotropy beneath southern Iberia from SKS splitting. Earth and Planetary Science Letters 273, 237–250.

Calvert, A., Sandvol, E., Seber, D., Barazangi, M., Roecker, S., Mourabit, T., Vidal, F., Alguacil, G., Jabour, N., 2000. Geodynamic evolution of the lithosphere and upper mantle beneath the Alboran region of the western Mediterranean: constraints from travel time tomography. Journal of Geophysical Research 105, 10,871–10,898.

Cambeses, A., 2011. Characterization of the volcanic centres at Zeneta and La Aljorra, Murcia: evidence of Minette formation by lamproite-trachyte magma mixing. (Master Thesis) University of Granada (249 pp.).

Carlier, G., Lorand, J.P., Liégeois, J.P., Fornari, M., Soler, P., Carlotto, V., Cárdenas, J., 2005. Potassic-ultrapotassic mafic rocks delineate two lithospheric mantle blocks beneath the southern Peruvian Altiplano. Geology 33, 601–604.

Cesare, B., Gómez-Pugnaire, M.T., 2001. Crustal melting in the alborán domain: constraints from xenoliths of the Neogene Volcanic Province. Physics and Chemistry of the Earth, Part A: Solid Earth and Geodesy 26, 255–260.

Cesare, B., Rubatto, D., Gómez-Pugnaire, M.T., 2008. Do extrusion ages reflect magma generation processes at depth? An example from the Neogene Volcanic Province of SE Spain. Contributions to Mineralogy and Petrology 157, 267–279.

Comas, M.C., Platt, J.P., Soto, J.I., Watts, A.B., 1999. The origin and tectonic history of the Alboran Basin: insights from Leg 161 results. Proceeding of the Ocean Drilling Program, Scientific Results 161, 555–580.

Conticelli, S., Guarnieri, L., Farinelli, A., Mattei, M., Avanzinelli, R., Bianchini, G., Boari, E., Tommasini, S., Tiepolo, M., Prelević, D., Venturelli, G., 2009. Trace elements and Sr–Nd–Pb isotopes of K-rich, shoshonitic, and calc-alkaline magmatism of the Western Mediterranean Region: genesis of ultrapotassic to calc-alkaline magmatic associations in a post-collisional geodynamic setting. Lithos 107, 68–92.

De Vicente, G., Cloetingh, S., Muñoz-Martín, A., Olaiz, A., Stich, D., Vegas, R., Galindo-Zaldívar, J., Fernández-Lozano, J., 2008. Inversion of moment tensor focal mechanisms for active stresses around the microcontinent Iberia: tectonic implications. Tectonics 27, TC1009. http://dx.doi.org/10.1029/2006TC002093.

Díaz, J., Gallart, J., Villaseñor, A., Mancilla, F., Pazos, A., Córdoba, D., Pulgar, J.A., Ibarra, P., Harnafi, M., 2010. Mantle dynamics beneath the Gibraltar Arc (western Mediterranean) from shear-wave splitting measurements on a dense seismic array. Geophysical Research Letters 37, L18304. http://dx.doi.org/10.1029/2010GL044201.

Dilek, Y., Altunkaynak, Ş., 2009. Geochemical and temporal evolution of Cenozoic magmatism in western Turkey: mantle response to collision, slab break-off, and lithospheric tearing in an orogenic belt. Geological Society, London, Special Publications 311, 213–233.

Duggen, S., Hoernle, K., Klügel, A., Geldmacher, J., Thirlwall, M., Hauff, F., Lowry, D., Oates, N., 2008. Geochemical zonation of the Miocene Alborán Basin volcanism (westernmost Mediterranean): geodynamic implications. Contributions to Mineralogy and Petrology 156, 577–593.

Duggen, S., Hoernle, K., Van Den Bogaard, P., Garbe-Schönberg, D., 2005. Post-collisional transition from subduction- to intraplate-type magmatism in the Westernmost Mediterranean: evidence for continental-edge delamination of subcontinental lithosphere. Journal of Petrology 46, 1155–1201.

Duggen, S., Hoernle, K., van den Bogaard, P., Harris, C., 2004. Magmatic evolution of the Alboran region: the role of subduction in forming the western Mediterranean and causing the Messinian Salinity Crisis. Earth and Planetary Science Letters 218, 91–108.

Faccenna, C., Piromallo, C., Crespo-Blanc, A., Jolivet, L., Rossetti, F., 2004. Lateral slab deformation and the origin of the western Mediterranean arcs. Tectonics 23, TC1012. http://dx.doi.org/10.1029/2002TC001488.

Férriz, F.J., Fernández-Soler, J.M., Cámara, F., 1994. Presencia de afloramientos de lamproitas en las proximidades de Moratalla y Cehegin (Murcia). Boletín de la Sociedad Española de Mineralogía 17, 231–239.

Fúster, J.M., Gastesi, P., Sagredo, J., Fermoso, M.L., 1967. Las rocas lamproíticas de SE de España. Estudios Geológicos 23, 35–69.

Galindo-Zaldívar, J., González-Lodeiro, F., Jabaloy, A., 1993. Stress and palaeostress in the Betic-Rif cordilleras (Miocene to the present). Tectonophysics 227, 105–126.

Galindo-Zaldívar, J., Jabaloy, A., González-Lodeiro, F., Aldaya, F., 1997. Crustal structure of the central sector of the Betic Cordillera (SE Spain). Tectonics 16, 18–37.
Garcia-Castellanos, D., Fernàndez, M., Torne, M., 2002. Modeling the evolution of the Guadalquivir foreland basin (southern Spain). Tectonics 21 (3), 1018. http://dx.doi.org/10.1029/2001TC001339.
Garcia-Castellanos, D., Villaseñor, A., 2011. Messinian salinity crisis regulated by competing tectonics and erosion at the Gibraltar arc. Nature 480, 359–363.
Gasparon, M., Rosenbaum, G., Wijbrans, J., Manetti, P., 2009. The transition from subduction arc to slab tearing: evidence from Capraia Island, northern Tyrrhenian Sea. Journal of Geodynamics 47, 30–38.
Govers, R., Wortel, M.J.R., 2005. Lithosphere tearing at STEP faults: response to edges of subduction zones. Earth and Planetary Science Letters 236, 505–523.
Govindaraju, K., Potts, P.J., Webb, P.C., Watson, J.S., 1994. 1994 Report on Whin Sill Dolerite Ws-E from England and Pitscurrie Microgabbro Pm-S from Scotland: assessment by one hundred and four international laboratories. Geostandards Newsletter 18, 211–300.
Gutscher, M.-A., Dominguez, S., Westbrook, G.K., Le Roy, P., Rosas, F., Duarte, J.C., Terrinha, P., Miranda, J.M., Graindorge, D., Gailler, A., Sallares, V., Bartolome, R., 2012. The Gibraltar subduction: a decade of new geophysical data. Tectonophysics 574–575, 72–91.
Gutscher, M.-A., Malod, J., Rehault, J.-P., Contrucci, I., Klingelhoefer, F., Mendes-Victor, L., Spakman, W., 2002. Evidence for active subduction beneath Gibraltar. Geology 30, 1071–1074.
Hale, A.J., Gottschaldt, K.-D., Rosenbaum, G., Bourgouin, L., Bauchy, M., Mühlhaus, H., 2010. Dynamics of slab tear faults: insights from numerical modelling. Tectonophysics 483, 58–70.
Hopp, J., Trieloff, M., Brey, G.P., Woodland, A.B., Simon, N.S.C., Wijbrans, J.R., Siebel, W., Reitter, E., 2008. $^{40}Ar/^{39}Ar$-ages of phlogopite in mantle xenoliths from South African kimberlites: evidence for metasomatic mantle impregnation during the Kibaran orogenic cycle. Lithos 106, 351–364.
Jabaloy-Sánchez, A., Fernández-Fernández, E.M., González-Lodeiro, F., 2007. A cross section of the eastern Betic Cordillera (SE Spain) according field data and a seismic reflection profile. Tectonophysics 433, 97–126.
Jerez-Mir, L., 1973. Geología de la Zona Prebética en la transversal de Elche de la Sierra y sectores adyacentes (provincias de Albacete y Murcia). (PhD Thesis) Universidad de Granada (749 pp.).
Julià, J., Mancilla, F., Morales, J., 2005. Seismic signature of intracrustal magmatic intrusions in the Eastern Betics (Internal Zone), SE Iberia. Geophysical Research Letters 32, L16304. http://dx.doi.org/10.1029/2005GL023274.
Kelley, S.P., Wartho, J.-A., 2000. Rapid kimberlite ascent and the significance of Ar–Ar ages in xenolith phlogopites. Science 289, 609–611.
Kuiper, K.F., Deino, A., Hilgen, F.J., Krijgsman, W., Renne, P.R., Wijbrans, J.R., 2008. Synchronizing rock clocks of Earth history. Science 320, 500–504.
Le Bas, M.J., Le Maitre, R.W., Streckeisen, A., Zanettin, B., 1986. A chemical classification of volcanic rocks based on the total alkali-silica diagram. Journal of Petrology 27, 745–750.
Leblanc, D., 1990. Tectonic adaptation of the External Zones around the curved core of an orogen: the Gibraltar Arc. Journal of Structural Geology 12, 1013–1018.
Leblanc, D., Olivier, P., 1984. Role of strike-slip faults in the Betic-Rifian orogeny. Tectonophysics 101, 345–355.
Lee, J.Y., Marti, K., Severinghaus, J.P., Kawamura, K., Yoo, H.S., Lee, J.B., Kim, J.S., 2006. A redetermination of the isotopic abundances of atmospheric Ar. Geochimica et Cosmochimica Acta 70, 4507–4512.
Liu, L., Stegman, D.R., 2012. Origin of Columbia River flood basalt controlled by propagating rupture of the Farallon slab. Nature 482, 386–389.
Lonergan, L., White, N., 1997. Origin of the Betic-Rif mountain belt. Tectonics 16 (3), 504–522.
Mancilla, F. de L., Stich, D., Berrocoso, M., Martín, R., Morales, J., Fernandez-Ros, A., Páez, R., Pérez-Peña, A., 2013. Delamination in the Betic Range: deep structure, seismicity, and GPS motion. Geology 41, 307–310.
Martínez-Martínez, J., Booth-Rea, G., Azañon, J., Torcal, F., 2006. Active transfer fault zone linking a segmented extensional system (Betics, southern Spain): insight into heterogeneous extension driven by edge delamination. Tectonophysics 422, 159–173.
Martín-Velázquez, S., De Vicente, G., Rodríguez-Pascua, M.A., Calvo, J.P., 1997. Análisis dinámico del sistema de desgarres NO-SE del Prebético de Albacete. Revista de la Sociedad Geológica de España 11, 369–382.
Mattei, M., Cifelli, F., Funiciello, F., Rossetti, F., Faccenna, C., 2007. Neogene tectonic evolution of the Betic Chain: insights from paleomagnetic, structural analyses, and laboratory models. Revista de la Sociedad Geológica de España 20, 273–285.
Mattei, M., Cifelli, F., Rojas, I.M., Crespo Blanc, A., Comas, M., Faccenna, C., Porreca, M., 2006. Neogene tectonic evolution of the Gibraltar Arc: new paleomagnetic constrains from the Betic chain. Earth and Planetary Science Letters 250, 522–540.
Maury, R.C., Fourcade, S., Coulon, C., El Azzouzi, M., Bellon, H., Coutelle, A., Ouabadi, A., Semroud, B., Megartsi, M., Cotten, J., Belanteur, O., Louni-Hacini, A., Piqué, A., Capdevila, R., Hernandez, J., Réhault, J.P., 2000. Post-collisional Neogene magmatism of the Mediterranean Maghreb margin: a consequence of slab breakoff. Comptes Rendus de l'Académie des Sciences de Paris 331, 159–173.
Mitchell, R.H., Bergman, S.C., 1991. Petrology of lamproites. Plenum Press, New York (450 pp.).
Montero, P., Bea, F., 1998. Accurate determination of 87Rb/86Sr and 147Sm/144Nd ratios by inductively-coupled-plasma mass spectrometry in isotope geoscience: an alternative to isotope dilution analysis. Analytica Chimica Acta 358, 227–233.
Murphy, D.T., Collerson, K.D., Kamber, B.S., 2002. Lamproites from Gaussberg, Antarctica: Possible Transition Zone Melts of Archaean Subducted Sediments. Journal of Petrology 43, 981–1001.
Nelson, D.R., 1992. Isotopic characteristics of potassic rocks: evidence for the involvement of subducted sediments in magma genesis. Lithos 28, 403–420.
Nocquet, J.-M., 2012. Present-day kinematics of the Mediterranean: a comprehensive overview of GPS results. Tectonophysics 579, 220–242.
Palano, M., González, P.J., Fernández, J., 2013. Strain and stress fields along the Gibraltar Orogenic Arc: constraints on active geodynamics. Gondwana Research 23, 1071–1088.
Peccerillo, A., Martinotti, G., 2006. The Western Mediterranean lamproitic magmatism: origin and geodynamic significance. Terra Nova 18, 109–117.
Pedrera, A., Ruiz-Constán, A., Galindo-Zaldívar, J., Chalouan, A., Sanz de Galdeano, C., Marín-Lechado, C., Ruano, P., Benmakhlouf, M., Akil, M., López-Garrido, A.C., Chabli, A., Ahmamou, M., González-Castillo, L., 2011. Is there an active subduction beneath the Gibraltar orogenic arc? Constraints from Pliocene to present-day stress field. Journal of Geodynamics 52, 83–96.
Pe-Piper, G., Piper, D.J.W., 2007. Neogene backarc volcanism of the Aegean: new insights into the relationship between magmatism and tectonics. Geological Society of America Special Papers 418, 17–31.
Pérez-Valera, L.A., Sánchez-Gómez, M., Fernández-Soler, J.M., Pérez-Valera, F., Azor, A., 2010. Diques de lamproítas a lo largo de la Falla de Socovos (Béticas orientales). Geogaceta 48, 151–154.
Platt, J.P., Allerton, S., Kirker, A., Mandeville, C., Mayfield, A., Platzman, E.S., Rimi, A., 2003a. The ultimate arc: differential displacement, oroclinal bending, and vertical axis rotation in the External Betic-Rif arc. Tectonics 22 (3), 1017. http://dx.doi.org/10.1029/2001TC001321.
Platt, J.P., Behr, W.M., Johanesen, K., Williams, J.R., 2013. The Betic-Rif arc and its orogenic hinterland: a review. Annual Review of Earth and Planetary Sciences 41, 313–357.
Platt, J.P., Whitehouse, M.J., Kelley, S.P., Carter, A., Hollick, L., 2003b. Simultaneous extensional exhumation across the Alboran Basin: implications for the causes of late orogenic extension. Geology 31, 251–254.
Pouchou, J.L., Pichoir, F., 1985. "PAP" Φ (pz) procedure for improved quantitative microanalysis. In: Armstrong, J.T. (Ed.), Microbeam Analysis. San Francisco Press, San Francisco, pp. 104–106.
Prelević, D., Foley, S.F., 2007. Accretion of arc-oceanic lithospheric mantle in the Mediterranean: evidence from extremely high-Mg olivines and Cr-rich spinel inclusions in lamproites. Earth and Planetary Science Letters 256, 120–135.
Prelević, D., Foley, S.F., Cvetković, V., 2007. A review of petrogenesis of Mediterranean Tertiary lamproites: a perspective from the Serbian ultrapotassic province. Geological Society of America Special Papers 418, 113–129.
Prelević, D., Foley, S.F., Romer, R., Conticelli, S., 2008. Mediterranean Tertiary lamproites derived from multiple source components in postcollisional geodynamics. Geochimica et Cosmochimica Acta 72, 2125–2156.
Reiners, P.W., Brandon, M.T., 2006. Using thermochronology to understand orogenic erosion. Annual Review of Earth and Planetary Sciences 34, 419–466.
Rosell, O., Martí, A., Marcuello, À., Ledo, J., Queralt, P., Roca, E., Campanyà, J., 2011. Deep electrical resistivity structure of the northern Gibraltar Arc (western Mediterranean): evidence of lithospheric slab break-off. Terra Nova 23, 179–186.
Rosenbaum, G., Gasparon, M., Lucente, F.P., Peccerillo, A., Miller, M.S., 2008. Kinematics of slab tear faults during subduction segmentation and implications for Italian magmatism. Tectonics 27, TC2008. http://dx.doi.org/10.1029/2007TC002143.
Rosenbaum, G., Lister, G.S., 2004. Neogene and Quaternary rollback evolution of the Tyrrhenian Sea, the Apennines, and the Sicilian Maghrebides. Tectonics 23, TC1013. http://dx.doi.org/10.1029/2003TC001518.
Rosenbaum, G., Lister, G.S., Duboz, C., 2002. Relative motions of Africa, Iberia and Europe during Alpine orogeny. Tectonophysics 359, 117–129.
Ruiz-Constán, A., Pedrera, A., Galindo-Zaldívar, J., Pous, J., Arzate, J., Roldán-García, F.J., Marin-Lechado, C., Anahnah, F., 2012. Constraints on the frontal crustal structure of a continental collision from an integrated geophysical research: the central-western Betic Cordillera (SW Spain). Geochemistry, Geophysics, Geosystems 13, Q08012. http://dx.doi.org/10.1029/2011GC003824.
Salvioli-Mariani, E., Venturelli, G., 1996. Temperature of crystallization and evolution of the Jumilla and Cancarix lamproites (SE Spain) as suggested by melt and solid inclusions in minerals. European Journal of Mineralogy 8, 1027–1039.
Sánchez-Gómez, M., Martínez-Sánchez, C., García-García, F., Peláez, J.A., Pérez-Valera, F., Martínez-Andreu, M., Pérez-Valera, L.A., 2011. Evidence for a 4700-2100 BC palaeoearthquake recorded in a fluvial-archaeological sequence of the Segura River, SE Spain. Quaternary International 242, 106–114.
Sanz de Galdeano, C., Buforn, E., 2005. From strike-slip to reverse reactivation: the Crevillente Fault System and seismicity in the Bullas-Mula area (Betic Cordillera, SE Spain). Geologica Acta 3, 241–250.
Schellart, W.P., 2004. Kinematics of subduction and subduction-induced flow in the upper mantle. Journal of Geophysical Research 109, B07401. http://dx.doi.org/10.1029/2004JB002970.
Seghedi, I., Szakács, A., Pacheco, A.H., Matesanz, J.-L.B., 2007. Miocene lamproite volcanoes in south-eastern Spain—an association of phreatomagmatic and magmatic products. Journal of Volcanology and Geothermal Research 159, 210–224.
Soto, J.I., Fernández-Ibáñez, F., Fernàndez, M., García-Casco, A., 2008. Thermal structure of the crust in the Gibraltar Arc: Influence on active tectonics in the western Mediterranean. Geochemistry, Geophysics, Geosystems 9, Q10011. http://dx.doi.org/10.1029/2008GC002061.
Spakman, W., Wortel, M.J.R., 2004. A tomographic view on western Mediterranean geodynamics. In: Cavazza, W., Roure, F., Spakman, W., Stampfli, G.M., Ziegler, P. (Eds.), The TRANSMED Atlas — the Mediterranean region from crust to mantle. Springer, Berlin Heidelberg, pp. 31–52.
Steiger, R.H., Jäger, E., 1977. Subcommission on geochronology: convention on the use of decay constants in geo- and cosmochronology. Earth and Planetary Science Letters 36, 359–362.

Sun, S.-S., McDonough, W.F., 1989. Chemical and isotopic systematics of oceanic basalts: implications for mantle composition and processes. Geological Society, London, Special Publications 42, 313–345.

Tommasini, S., Avanzinelli, R., Conticelli, S., 2011. The Th/La and Sm/La conundrum of the Tethyan realm lamproites. Earth and Planetary Science Letters 301, 469–478.

Torres-Ruiz, J., Pesquera, A., Gil-Crespo, P., Velilla, N., 2003. Origin and petrogenetic implications of tourmaline-rich rocks in the Sierra Nevada (Betic Cordillera, southeastern Spain). Chemical Geology 197, 55–86.

Toscani, L., Contini, S., Ferrarini, M., 1995. Lamproitic rocks from Cabezo Negro de Zeneta: brown micas as a record of magma mixing. Mineralogy and Petrology 55, 281–292.

Turner, S.P., Platt, J.P., George, R.M.M., Kelley, S.P., Pearson, D.G., Nowell, G.M., 1999. Magmatism associated with orogenic collapse of the betic–Alboran Domain, SE Spain. Journal of Petrology 40, 1011–1036.

Vasconcelos, P.M., Onoe, A.T., Kawashita, K., Soares, A.J., Teixeira, W., 2002. $^{40}Ar/^{39}Ar$ geochronology at the Instituto de Geociências, USP: instrumentation, analytical procedures, and calibration. Anais da Academia Brasileira de Ciências 74, 297–342.

Vaughan, A.P.M., Scarrow, J.H., 2003. K-rich mantle metasomatism control of localization and initiation of lithospheric strike-slip faulting. Terra Nova 15, 163–169.

Venturelli, G., Capedri, S., Di Battistini, G., Crawford, A., Kogarko, L.N., Celestini, S., 1984. The ultrapotassic rocks from southeastern Spain. Lithos 17, 37–54.

Wortel, M.J.R., Spakman, W., 2000. Subduction and slab detachment in the Mediterranean-Carpathian region. Science 290, 1910–1917.